Exploring the possibilities of increasing energy density and efficiency in rechargeable batteries
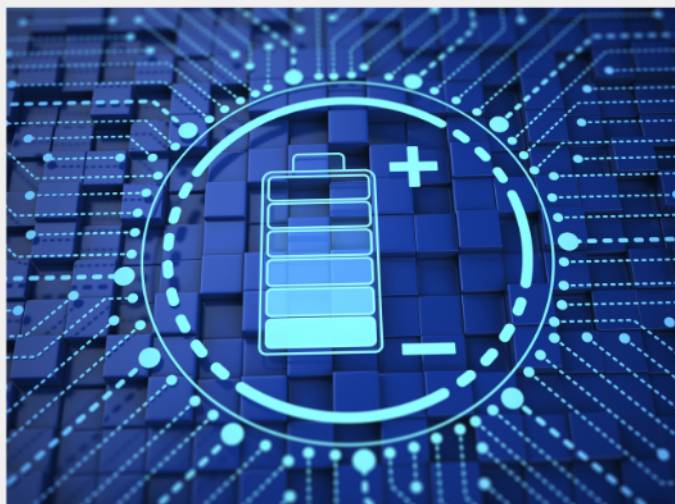
The exponential rise in the need for better, more efficient power sources has sparked an incredible amount of research into batteries. A primary focus of research has been increasing the energy density of batteries, as it allows for lighter, more portable storage of energy. Lithium-ion batteries, for example, have a much higher energy density than conventional lead-acid batteries and can be used for various purposes, such as in electric vehicles.

This article collection provides a comprehensive list of references for new methods and technologies for increasing the energy density of batteries.

Metrohm

WILEY

Room-Temperature Exceptional-Point-Driven Polariton Lasing from Perovskite Metasurface

M.A. Masharin, A.K. Samusev, A.A. Bogdanov, I.V. Iorsh, H.V. Demir, and S.V. Makarov*

Excitons in lead bromide perovskites exhibit high binding energy and high oscillator strength, allowing for a strong light-matter coupling regime in the perovskite-based cavities localizing photons at the nanoscale. This opens up the way for the realization of exciton-polariton Bose–Einstein condensation and polariton lasing at room temperature – the inversion-free low-threshold stimulated emission. However, polariton lasing in perovskite planar photon cavities without Bragg mirrors has not yet been observed and proved experimentally. In this study, perovskite metasurface is employed, fabricated with nanoimprint lithography, supporting so-called exceptional points to demonstrate the room-temperature polariton lasing. The exceptional points in exciton-polariton dispersion of the metasurface appear upon optically pumping in the nonlinear regime in the spectral vicinity of a symmetry-protected bound state in the continuum providing high mode confinement with the enhanced local density of states beneficial for polariton condensation. The observed lasing emission possesses high directivity with a divergence angle of 1° over one axis. The employed nanoimprinting approach for solution-processable large-scale polariton lasers is compatible with various planar photonic platforms suitable for on-chip integration.

1. Introduction

Exciton-polaritons are bosonic hybrid part-light, part-matter quasiparticles, which have attracted tremendous attention thanks to a set of remarkable properties.[1] The photon fraction provides a small effective mass and long decoherence time, whereas the excitonic fraction enables strong optical nonlinearity caused by the Coulomb interaction between quasiparticles. The unique combination of the properties allows the realization of Bose–Einstein condensation – the state, where bosons are accumulated in one quantum state exhibiting collective coherence on a macroscopic scale.[2,3] In the case of non-equilibrium polariton systems, it turns to the low-threshold polariton lasing, which does not require inversion of population.[4] The most widely used photon cavity for polariton systems is distributed Bragg reflectors since such a cavity supports high-quality optical states with parabolic dispersion, which can be measured directly with the angle-resolved spectroscopy method.[5] The strong light-matter coupling regime and polariton lasing were already demonstrated for many materials,[3,6,7] even at room temperature.[8–11] However, polariton lasers can be also realized in other planar cavities, such as metasurfaces, which have recently attracted high attention thanks to their unique properties.[12]

Metasurfaces can be classified by their functionality and design.[13] If the operating wavelength is longer or comparable with the metasurface period, light can propagate along the metasurface, providing a non-local response.[13] In such non-local metasurfaces, it is possible to realize high-Q resonances with large optical confinement without exploiting

M.A. Masharin, H.V. Demir
UNAM–Institute of Materials Science and Nanotechnology
Department of Electrical and Electronics Engineering
Department of Physics
Bilkent University
Ankara 06800, Turkey

M.A. Masharin, A.K. Samusev, A.A. Bogdanov, I.V. Iorsh, S.V. Makarov
ITMO University
School of Physics and Engineering
St. Petersburg 197101, Russia
E-mail: makarov_sergey_vl@mail.ru

A.K. Samusev
Experimentelle Physik 2
Technische Universität Dortmund
44227 Dortmund, Germany

A.A. Bogdanov, S.V. Makarov
Qingdao Innovation and Development Center
Harbin Engineering University
Qingdao, Shandong 266000, China

I.V. Iorsh
Department of Physics
Bar-Ilan University
Ramat Gan 52900, Israel

H.V. Demir
LUMINOUS! Center of Excellence for Semiconductor Lighting and Displays
School of Electrical and Electronic Engineering
School of Physical and Materials Sciences
School of Materials Science and Engineering
Nanyang Technological University
Singapore 639798, Singapore

The ORCID identification number(s) for the author(s) of this article can be found under https://doi.org/10.1002/adfm.202215007.

DOI: 10.1002/adfm.202215007

Bragg mirrors. The high-Q resonances originating from the destructive interference of counterpropagating waves are called bound states in the continuum (BICs).[12,14,15] By varying the metasurface design it is possible to precisely control the spectral position and radiative lifetime of the optical resonance. In opposite to Bragg mirrors, a planar metasurface can be fabricated with substantially simplified techniques, such as nanoimprint lithography. Moreover, if the metasurface design provides the BICs strongly coupled with the exciton resonance, polariton condensation state in a nonlinear regime can be realized.[14,16]

However, there is another specific state in metasurfaces for the efficient polariton accumulation. When two hybrid optical modes are not split but degenerated at some point in the dispersion curve, it might result in the emergence of exceptional points (EPs).[17] These exotic states are very sensitive to parameter variations and were also observed in a rich variety of systems including whispering gallery mode resonators,[18] metasurfaces,[17] and coupled waveguides.[19] EPs can enhance lasing emission and allow to control the lasing directivity.[18,20,21] Recently, it was also shown that EPs provide the enhanced local density of the states (LDOS), scaling with a square of the Purcell factor.[22,23] If EPs appear on a polariton branch, this causes a strong enhancement of the boson scattering probability to this state, which can lead to the polariton accumulation in a nonlinear regime, resulting in the polariton lasing.[24,25]

In turn, halide perovskites are one of the most promising candidates to be an active medium for the metasurface-based polariton lasers. This group of materials was proved to be a promising photo-active material for photovoltaics and optoelectronics.[26,27] Moreover, its outstanding physical properties such as relatively high exciton binding energy and oscillator strength,[28] as well as high defect tolerance,[29] allow for realizing a strong light-matter coupling regime in photonic cavities and even non-equilibrium polariton Bose-Einstein condensation at room temperature.[9,10,30–33] Moreover, solution-based methods of synthesis, combined with a high refractive index of the synthesized materials, and their scalable nanostructuring techniques, such as direct laser ablation,[34] nanoimprint lithogrpahy,[35] and self-assembly methods,[36] open the way to apply them in planar metasurfaces, supporting high-Q polariton states and avoiding vertical Bragg cavities.[36–39] Although the perovskites were used in different laser designs[40] including surface-emitting distributed feedback lasers,[41–43] while polariton lasing in halide perovskite metasurfaces has not been yet observed experimentally.

In this work, we experimentally demonstrate room-temperature exciton-polariton lasing in the perovskite non-local metasurface (see the design in **Figure 1**a). The polariton lasing is based on the EPs that appear in the spectral vicinity of a symmetry-protected BIC under a non-resonant optical pump in the nonlinear regime (Figure 1b). The observed lasing emission is characterized by unidirectional propagation along the metasurface periodicity direction and broad distribution along the perpendicular axis in the range of 11 degrees from the normal. Thanks to the dispersion of polariton modes in the perovskite metasurface, the EPs turn into curves in the Fourier plane, resulting in the observed lasing emission directivity.

2. Results and Discussion

2.1. Fabrication and Characterization of the Perovskite Metasurface

One of the most important advantages of perovskites is the solution methods of synthesis, which provide the low-cost fabrication of these materials and make them very promising for real-world applications.[44] Also, halide perovskites are known as an admirable material for nanoimprint lithography due to their crystal lattice softness, which is also very suitable for further scaling.[35,45] We use both techniques for the fabrication of $MAPbBr_3$ metasurface, which demonstrate the high quality of the morphology and resulting optical modes (see Experimental Section and Supporting Information for details).

The perovskite metasurface represents a periodic grating, controlled by the mold, with a period of 320 nm, which is determined from the scanning electron microscopy (SEM) image, shown in Figure 1c. The grating ridge height is around 20 nm, the comb width is around 160 nm, and the full sample thickness from the substrate to the comb top is around 75 nm, according to the atomic force microscopy (AFM) measurements shown in Figure 1d. The extracted grating profiles along the x-axis are shown in Figure S2 (Supporting Information). We also fabricate the sample with a thickness of 65 nm by increasing the spin-coating rotation speed. It is observed that perovskite grains in the nanoimprinted structure are not deformed or damaged and the resulting structure possesses high crystallinity. According to our observations, due to the room-temperature nanoimprinting process applied during the intermediate phase, the crystallization process continues in the mold geometry during the nanoimprint process. Moreover, after the annealing, the structure stiffens and cannot be modified by the polycarbonate mold at room temperature.

Based on the extracted perovskite non-local metasurface geometry parameters and the $MAPbBr_3$ refractive index, studied before,[46] we estimate the wavevectors of leaky mode resonances with linear polarization co-direct with a groove of metasurface (TE polarization) as a function of the photon energy by the Fourier Modal Method (FMM)[47] for the sample with a thickness of 75 nm. As the estimations well correlate with the experimentally measured angle-resolved reflection spectrum at $k_y/k_0 = 0$ (Figure S3, Supporting Information), we simulate the full dispersion surface of the perovskite metasurface shown in Figure 1e (see Section 1, Supporting Information). In the current geometry, the modes with opposite x-components of the group velocities intersect at the curve, located in the plane of $k_x/k_0 = 0$. Note that, in the range of $|k_y/k_0| < 0.2$, spectral positions of the mode intersection points, shown as a green line in Figure 1e, vary in the range of 3 meV. As the mode linewidth of ≈ 6 meV exceeds this value, the intersection set of points represents a straight line without any energy dependence. Also, the leaky modes are studied in the region of the exciton resonance and, therefore, are affected by it (Figure S4, Supporting Information). The curvature of the leaky mode at constant k_y/k_0 from the linear dependence to the exciton resonance asymptote is a sign of exciton-polariton behavior.[48]

**ADVANCED
SCIENCE NEWS**

www.advancedsciencenews.com

**ADVANCED
FUNCTIONAL
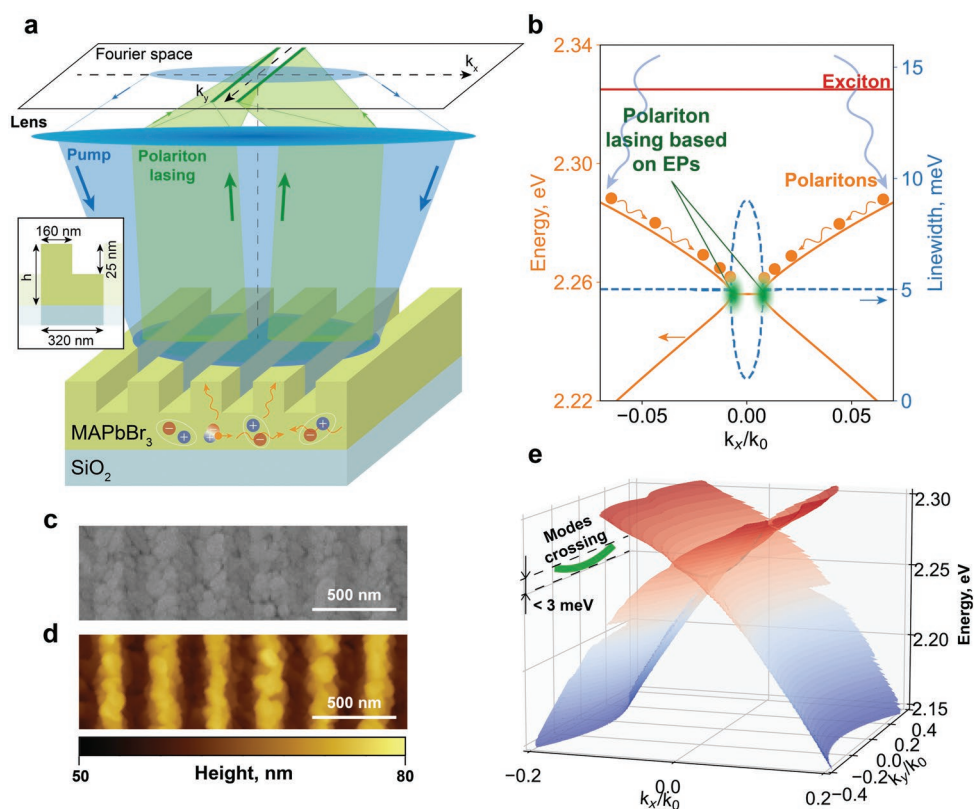MATERIALS**

www.afm-journal.de

Figure 1. Concept of the polariton lasing enabled by the exceptional points in the perovskite metasurface. a) Sketch of polariton lasing enhanced by EPs in perovskite metasurface, where femtosecond laser pumps the MAPbBr₃ metasurface and leaky modes strongly coupled to the exciton resonance, resulting in exciton-polaritons, cause the polariton lasing, which is observable in Fourier space of the optical setup. The stimulated emission arises at the in-plane wavevector k_x close to zero in a wide range of k_y. b) Sketch of the exciton-polariton dispersion for the leaky modes in the perovskite metasurface. The solid red line shows the exciton resonance, and the orange line shows the polariton dispersion. Blue dashed lines represent the linewidth of the polariton branches. The blue arrows represent carrier relaxation after the non-resonant pump into the polariton states. The range arrows illustrate the stimulated polariton relaxation into the localized state. The green ellipses correspond to the polariton lasing, based on exceptional points. c) SEM and d) AFM images of the fabricated perovskite metasurface. The geometrical parameters obtained from the AFM and SEM data are shown in the inset of (a). e) The dispersion surface of the studied metasurface calculated by the Fourier Modal Method. Pseudo-colors correspond to the energy. The black solid line shows the crossing of the counter-propagating modes at $k_x/k_0 = 0$ for various k_y/k_0. Its projection is shown with the green line and is limited to the angles $k_x/k_0 \approx 0.2$, used in the experimental studies. The energy variation in the modes crossing does not exceed 3 meV in the considered range of k_y/k_0.

2.2. Strong Light-Matter Coupling Regime in Perovskite Metasurface

In order to confirm the strong light-matter coupling regime, we perform angle-resolved reflectance and photoluminescence measurements (see Experimental Section for details). The angle-resolved measurements at $k_y/k_0 = 0$ in TE polarization are performed for two samples with thicknesses of 65 and 75 nm, but having identical pitch and modulation depth, shown in **Figures 2**a,b. The samples are labeled as an "ASE sample" and "lasing sample", respectively, as they provide spectrally broad and narrow stimulated emission, respectively, under a non-resonant femtosecond pump. The difference in the sample thickness causes the variation in the real $E_{LP}(k_x)$ and imaginary $\gamma_{LP}(k_x)$ parts of leaky modes dispersions (Figure 2a,b) and linewidths (Figure 2c,d). Both dispersions demonstrate the curvature of the mode near the exciton resonance, which is the sign of the exciton-polaritons, as was mentioned above. In the absence of the excitonic resonance, the leaky mode has nearly

linear behavior as a function of k_x/k_0 in the spectral range of interest and can be considered as an uncoupled cavity photon (see Figure S4 Supporting Information). The observed polariton dispersion can be described by the two-coupled oscillator model:[48]

$$E_{LP}(k_x) = \frac{E_X + E_C(k_x)}{2} - i\frac{\gamma_X + \gamma_C}{2} - \frac{1}{2}\sqrt{\left[\left(E_C(k_x) - E_X\right) - i(\gamma_C - \gamma_X)\right]^2 + 4g_0^2} \tag{1}$$

there $E_{LP}(k_x)$ stands for the complex energy dispersion of the lower polariton branch; E_X and γ_X stand for the real and imaginary parts of the exciton resonance, respectively; $E_C(k_x)$ and γ_C stand for the dispersion and linewidth of the uncoupled cavity photon mode, respectively; and g_0 stands for the light-matter coupling coefficient. It should be noted, that we do not observe the upper polariton branch due to the strong optical absorption in the spectral region higher than the exciton resonance.[49]
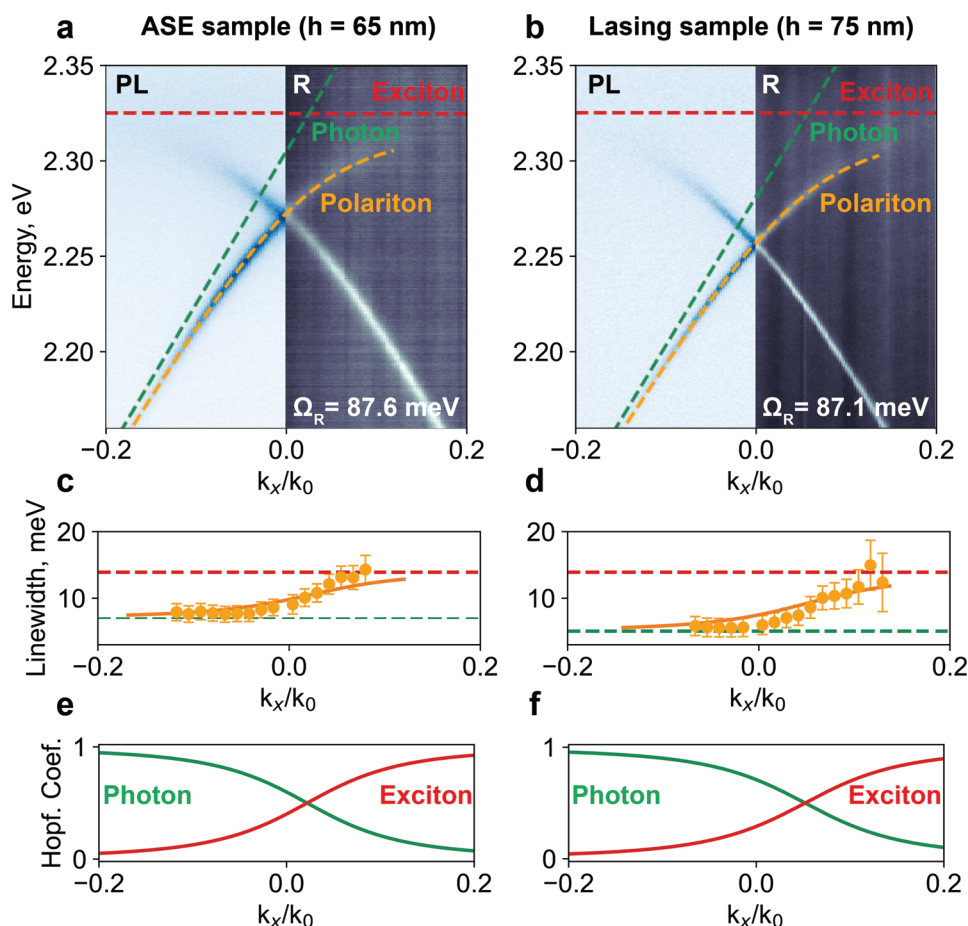
ADVANCED
SCIENCE NEWS
www.advancedsciencenews.com

ADVANCED
FUNCTIONAL
MATERIALS
www.afm-journal.de

Figure 2. Fitting of the exciton-polariton branch for the samples without and with exceptional points, respectively. a,b) Measured angle-resolved reflection and PL spectra for the ASE sample and lasing sample. Red dashed lines correspond to the exciton resonance, green dashed lines correspond to the estimated uncoupled photon cavity dispersion, and orange dashed lines correspond to the exciton-polariton dispersions, estimated by the two-coupled oscillators model.[48] The resulting Rabi splitting is equal to 87.6 and 87.1 meV, respectively. c,d) Linewidths extracted from experimental data are shown by orange dots. Estimated exciton linewidth is shown by red dashed lines and uncoupled cavity photon linewidths are shown by green dashed lines. The solid orange lines show the result of the two-coupled model fitting. The error bars show the root-mean-squared error of the extracted mode linewidths. e,f) Estimated Hopfield coefficients based on the fitted two-coupled model parameters. The red line corresponds to the exciton fraction $|X|^2$ and the green line corresponds to the photon fraction $|C|^2$ (see Section 2 Supporting Information).

Nevertheless, Rabi splitting, which is identified as a difference between lower and upper polariton branches in the intersection point $E_X = E_C(k_x)$ can be estimated as

$$\Omega_R = \sqrt{4g_0^2 - (\gamma_C - \gamma_X)^2} \qquad (2)$$

If the coupling coefficient exceeds the half-difference of the linewidths (i.e., $g_0 > (\gamma_C - \gamma_X)/2$) and the value of Rabi splitting exceeds the half-sum (i.e., $\Omega_R > (\gamma_C + \gamma_X)/2$) strong light-matter coupling regime appears.[48]

In order to estimate the coupling coefficient g_0 and check if the system is in a strong light-matter coupling regime, we extract the leaky mode dispersion and linewidths $E_{LP}(k_x)$ from the measured angle-resolved PL spectra by the fitting of the mode resonances at each k_x/k_0 by the Lorentz peak function. As uncoupled photon cavity mode dispersion $E_C(k_x)$ in the metasurface is considered to have linear behavior with respect to the k_x/k_0, we estimate it by the linear approximation of the leaky mode in the spectral region far from the exciton resonance

(1.9–2.0 eV). The linewidth γ_C is estimated from the leaky mode linewidth in the same spectral region and is equal to 7 meV for the ASE sample and 5 meV for the lasing sample. The coupling coefficient g_0 is determined as an optimized parameter in the fitting by the two-coupled oscillator model. In the same way, the exciton resonance E_X and linewidth γ_x are also determined as optimized parameters and well correspond to the previous estimations.[50,51] It should be noted that this approach of the exciton level estimation well predicts the exciton resonance in comparison with other methods.[52] The result of the complex mode dispersion fitting by the two-coupled oscillator model is shown in Figure 2a–d. The real part of the $E_{LP}(k_x)$, shown by the dashed lines in Figure 2a,b well corresponds to the experimental data, as well as the imaginary part shown in Figure 2c,d. The coupling coefficient g_0 is estimated to be equal to 43.8 meV for both samples, but Ω_R is 87.6 meV for the ASE sample and 87.1 meV for the lasing sample. As the coupling coefficient depends on the material properties and electric field localization, it is the same for both samples, but the difference is in the

**ADVANCED
SCIENCE NEWS**

www.advancedsciencenews.com

**ADVANCED
FUNCTIONAL
MATERIALS**

www.afm-journal.de

photon cavity linewidth, which causes the difference in Ω_R. As for both samples, g_0 exceeds the exciton and photon linewidths half-difference, which is around 7 and 9 meV, as well as Ω_R is larger than the half-sum, which is around 9.5 and 10.5 meV, we confirm that in the studied perovskite metasurface, the strong light-matter coupling regime is achieved.

As exciton-polaritons are hybrid light-matter quasiparticles, there can be estimated a fraction of the exciton $|X|^2$ and photon $|C|^2$ in the polariton wavefunction, which is also called Hopfield coefficients (see Section 2, Supporting Information).[48] The estimated coefficients as a function of the k_x/k_0 are shown in Figure 2e,f. At the Γ-point, where $k_x/k_0 = 0$, the exciton fraction $|X|^2$ is around 0.4 in the ASE sample and around 0.29 in the lasing sample. On the one hand the higher the exciton fraction, the larger the optical nonlinear effects and exciton optical gain, but on the other hand, with a higher exciton fraction, nonradiative losses rise, which reduces the polariton lifetime. As a result, there exists a balance between these two effects on the polariton branch, where polaritons may efficiently accumulate and cause polariton stimulation in this state after some threshold.[24,25]

2.3. Polariton-Mediated ASE and Lasing in Perovskite Metasurface

To study the stimulated emission of the samples, we perform angle-resolved PL measurements by varying the pump fluence. Under the pump fluences around 6 μJ cm^{-2} and lower we observe linear emission regime, coming from the polariton branches and background PL, which is observed from the unstructured film (**Figure 3**a,b). The intensity of the background PL spectrum is much lower than the emission intensity of polariton modes and it is hidden in figures, however, it is still noticeable (see Figure S7, Supporting Information). With increasing the pump fluence, we observe a blueshift and broadening of the polariton modes, and after the pump threshold, we observe stimulated emission. In the case of the ASE sample, broad enhanced amplified spontaneous emission (ASE) on the polariton branch for k_x/k_0 in the range of 0.03–0.05 is observed, where the exciton Hopfield coefficient is around 0.3. But in the case of the lasing sample, we observe spectrally narrow emission with $k_x/k_0 \approx 0$, corresponding to the polariton accumulation in EPs. Since the metasurface with a height of $h = 65$ nm provides the spectral position of modes crossing closer to the exciton resonance in comparison with $h = 75$ nm, the nonradiative optical losses are higher (see Supporting Information for details). Also, the radiative losses are increased due to the higher relative modulation (see Supporting Information for details). Therefore, the full losses of the optical resonance at $k_x/k_0 = 0$ cannot be compensated with optical gain to achieve EPs and hence provide only ASE.

With increasing the pump fluence ASE shifts to the red region along the polariton branch and spectrally broadens (Figure 3a). Meanwhile, the lasing emission increases in intensity, broads, and slightly shift to the blue region (Figure 3b). The reason for the observed effect is supposed to be in the origin of the polariton relaxation.[25,27] In the case of the ASE, the accumulated polaritons in a nonlinear regime scatter to

the lower energies, as there does not exist a state where a large number of polaritons can be accumulated. However, in the lasing sample, in a nonlinear regime, there appear the specific states at the $k_x/k_0 \approx 0$, where the polariton condensation with a narrow lasing emission is achieved. As was mentioned above, the states are supposed to be the EPs, which are caused by the stimulated emission and will be described in detail below.

In the real space (Figure 3c), the ASE emission is characterized as high-intensive spots with speckles on the left and right sides from the pump spot center with a wide distribution over the y-axis. Meanwhile, the lasing emission has a narrow distribution over the y-axis (Figure 3d). In the Fourier space, ASE is almost uniformly distributed over the polariton branches, showing isofrequency contours in the range of the ASE spectral center (Figure S6, Supporting Information). However, the lasing emission is localized along the $k_x/k_0 = 0$ with almost a straight line with respect to the k_y/k_0 (see inset in Figure 3d). As was shown before, the spectral position of the modes intersection is considered as a constant for the $|k_y/k_0| < 0.2$ (Figure 1e), and therefore EPs are supposed to exist over the whole of this stripe. As a result, polaritons accumulate equiprobably over the stripe and produce the unidirectional lasing. It should be noted that in the Fourier space image of the lasing, we detect a characteristic dip in the lasing intensity exactly around $k_x/k_0 = 0$ because of the symmetry mismatching between the BIC and plane wave propagating normally. The EPs appearing in the nonlinear regime are slightly detuned from the $k_x/k_0 = 0$. It is not observed in the spectra of the lasing emission, shown in Figure 3b, because of the limited resolution over k_x/k_0, and will be shown further.

In order to analyze the ASE and lasing emission as a function of the pump fluence in detail, we fit it by the Lorentzian function. As ASE is not localized in some k_x/k_0, we integrate the emission overall k_x/k_0 for the analysis (solid red markers in Figure 3e–g), and for the lasing sample, we study the emission at the $k_x/k_0 = 0$ (solid blue markers in Figure 3e–g). However, in order to compare the mode parameters of the ASE sample before the threshold, we also fit the mode at $k_x/k_0 \approx 0.03$, corresponding to the maximum of the ASE at the pump threshold (empty red markers in Figures 3f,g). Both ASE and lasing emission show the S-curve shape of dependence of the emitted signal intensity as a function of the pump fluence (Figure 3e). The pump threshold of the ASE is estimated as 46 μJ cm^{-2} and of the lasing emission as 30 μJ/cm^{-2}. The difference in the pump threshold is attributed to the different losses of the samples, mentioned above and also the existence of the EPs in the lasing sample. The EPs appear in the system in a nonlinear regime when polariton relaxation provides the optical gain and does not require overcoming all losses (see Section 3, Supporting Information). When it appears, the probability of the polaritons scattering in this state dramatically increases, which reduces the lasing threshold. Also, the lasing sample shows an enhanced increase in the intensity after the threshold by more than three orders of magnitude in comparison with the one order observed in the ASE sample. This can be explained by the dramatically increased rate of polariton stimulation to EPs in the nonlinear regime.[24] The polaritons reaching this state radiatively recombine, producing lasing emission in a time scale much shorter than a non-radiative lifetime,[53] which thus
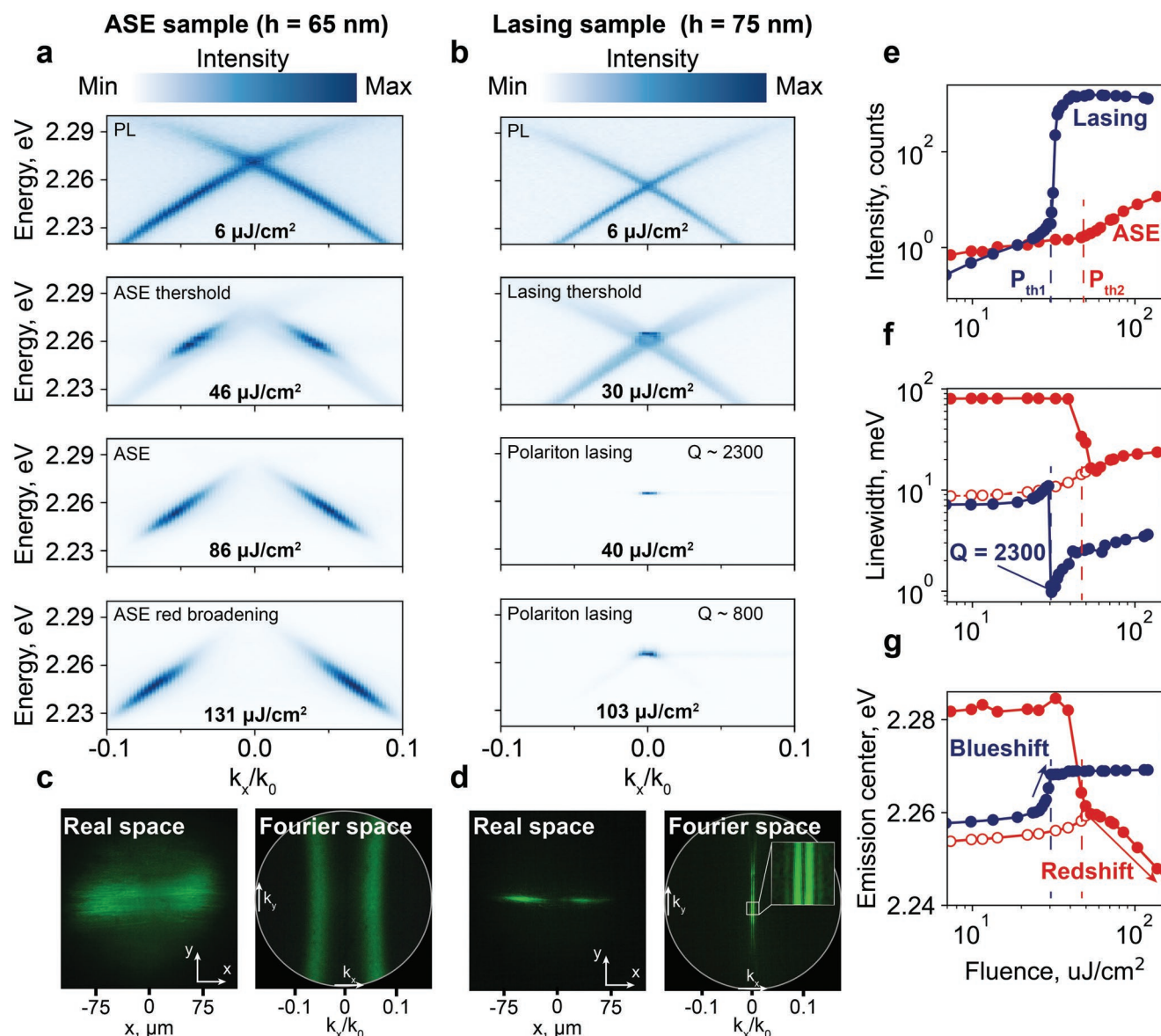
ADVANCED
SCIENCE NEWS
www.advancedsciencenews.com

ADVANCED
FUNCTIONAL
MATERIALS
www.afm-journal.de

Figure 3. Polariton-mediated ASE and lasing in the samples without and with exceptional points, respectively. a) Angle-resolved emission spectra obtained from ASE sample under different pump fluences. Linear PL is observed at 6 μJ cm^{-2}, near 46 μJ cm^{-2} intense broadband ASE peak appears, which is localized in the polariton branch and is of the polariton nature. With increasing the pump fluence, the ASE peak rises in intensity and broadens towards the red region due to the polariton relaxation. b) Similar measurements are provided for the lasing sample. Under the pump fluence threshold of 30 μJ cm^{-2}, narrow lasing emission appears around $k_x/k_0 = 0$, which rises in intensity and broadens with increasing pump fluence. The origin of the lasing in the polariton accumulation in the EPs c) The images of the ASE in the real and Fourier space, obtained at 86 μJ cm^{-2}. Fourier space shows high-intensive isofrequency at the ASE spectral energies. d) The images of the lasing emission, which are obtained at 40 μJ cm^{-2} of pump fluence. The sample shows narrow lasing emission in real space and narrow plane emission in Fourier space along k_x. The characteristic dip in intensity at the $k_x = 0$ is supposed to be due to the symmetry mismatching between the BIC and the plane wave propagating normally away from the sample. e) The intensity of the emission as a function of the pump fluence. Solid red and blue lines with solid markers show the intensity of the emission observed in the ASE and lasing samples, respectively. f) Linewidths of the ASE and lasing emission peaks as a function of the pump fluence. Solid red markers correspond to the linewidth of the integrated emission from the ASE sample over the k_x/k_0. Empty red markers correspond to the mode linewidths of the ASE sample at $k_x/k_0 = 0.029$. Solid blue markers correspond to the mode linewidth of the lasing sample at $k_x/k_0 = 0$. g) Extracted emission central energy of the integrated ASE sample, mode of the ASE sample, and mode of the lasing sample, shown as red solid markers, red empty markers, and blue solid markers, respectively.

strongly suppresses non-radiative recombination. The slight decrease of the lasing intensity at higher fluence can appear due to the further increase of the optical gain, leading to the disappearance of the polariton mode degeneracy and the fade of the exceptional points. Also, it can be attributed to Auger recombination or additional heating of the material.[54]

The integrated emission of the ASE sample in the linear regime before the threshold represents a broad spectrum with

ADVANCED
SCIENCE NEWS
www.advancedsciencenews.com

ADVANCED
FUNCTIONAL
MATERIALS
www.afm-journal.de

a linewidth around 80 meV and a center around 2.28 eV, as shown in Figures 3f and 3g by red solid markers. It should be noted that the estimated linewidth here is broadened with respect to the background PL spectrum, because the leaky modes enhance the outcoupled emission in the red region (see Figure S7, Supporting Information). At the threshold, the linewidth rapidly drops to the values of the mode linewidth (shown as red empty markers), as well as the emission center, because the ASE is strongly localized and enhanced by the polariton mode as it is shown in Figure 3a. It should also be noted that exactly before the threshold the center of the mode slightly shifts to the blue region, which is attributed to the non-linear polariton blueshift under the non-resonant pump.[6,16] With increasing the pump fluence, ASE spectrum broadens and shifts to the red region, because of the polariton relaxation discussed above. The lasing sample exhibits the mode linewidth of around 6 meV before the threshold with a spectral center energy of 2.258 eV. With further elevating the pump fluence, the mode shifts to the blue region by a value of 10 meV and broadens due to the polariton–polariton interaction.[6,45,52] Around the threshold, narrow lasing emission appears with a linewidth of around 1 meV corresponding to a Q-factor of 2300. With further increasing the pump fluence, the lasing mode broadens and slightly shifts to the blue region. The broadening is supposed to be due to the temporal changing of the lasing center peak during the emission. The blueshift of the lasing

peak is determined by the number of polaritons. After the high-intensity pump pulse is absorbed, the formed polaritons shift the polariton branch to the blue region and the lasing emission appears. When the polaritons annihilate, producing the lasing emission, the number of polaritons reduces and the branch starts to return back to its initial spectral position. As a result, we observe broadened integrated-over-time lasing spectra. This assumption was previously confirmed by the temporal resolution of the lasing emission in polariton systems with a streak-camera.[16,53]

2.4. Observation of the EPs in the Lasing Regime

To confirm the presence of the EPs in the stimulated emission of the lasing sample, we increase the magnification of the BFP image and transferred it to the spectrometer imaging CCD to increase the angular resolution over k_x/k_0. The angle-resolved spectra with the increased resolution measured for different pump fluences with logarithmic scale in the pseudocolor are shown in **Figure 4**a. Under the low pump fluence around 6 μJ cm^{-2}, we observe a slight enhancement of the spontaneous emission near the $k_x/k_0 = 0$, which can be caused by the enhanced spontaneous emission, also reported in ref. [55]. At the pump threshold around 30 μJ cm^{-2}, polaritons start to interact with each other, which leads to the polariton branch
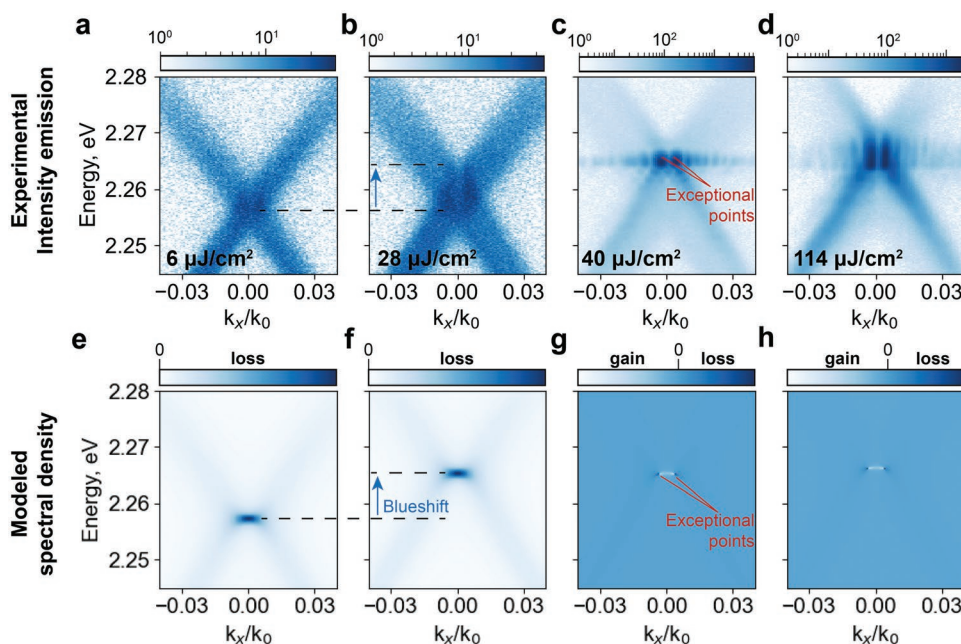

Figure 4. The observation of exceptional points in the lasing regime. a–d) Measured angle-resolved spectra of the lasing sample, obtained with enhanced resolution over a k_x/k_0 axis at $k_y/k_0 = 0$. In the linear PL spectrum, obtained under pump fluence lower than 6 μJ cm^{-2}, we observe enhanced spontaneous emission near the $k_x/k_0 = 0$, which is attributed to the EPs.[22,55] With the increase of pump fluence, we observe two lasing spots and a dark spot at $k_x/k_0 = 0$, which was barely visible in Fourier image in Figure 3b, which rises in intensity with the increase of the pump fluence. At 114 μJ cm^{-2} we observe the polariton lasing blueshift, due to the polariton–polariton interaction, and also spectral broadening discussed in the text in detail. e–h) Modeled spectral density of the studied perovskite metasurface lasing sample corresponding to the following regimes: (e) linear regime in the absence of optical gain, originating from the polariton stimulation, where the simulated quantity corresponds to the emission, observed in the experiment; (f) linear regime with blueshifted polariton branches due to the polariton–polariton interaction under pump fluences around 28 μJ cm^{-2}; (g) stimulated regime calculated by subtracting the gain profile (see Section 3, Supporting Information), where the change of the sign of the spectral density corresponds to the onset of the EPs providing enhanced LDOS; (h) corresponds to the system with an enhanced gain profile and slightly shifted polariton branch, as it is observed in the experiment at the highest fluence values.

blueshift and polariton stimulated scattering to the lower energies. The latter causes the polariton accumulation in the spectral region of observed ASE and provides the optical gain for leaky modes. As a result, when the critical values of the optical gain are achieved, EPs appear, and we observe two distinguished lasing spots near the $k_x/k_0 = 0$ (Figure 4c). Thanks to the enhanced LDOS, polaritons occupy these states, which leads to the polariton lasing. With increasing the pump fluence, we observe the increase of the lasing peak intensity and then broadening and the blueshift mentioned above (Figures 4c,d). In the logarithmic scale, scattered lasing signals over all k_x/k_0 are observed, which are attributed to the scattering on the sample impurities and grain boundaries. Also, around fluence 114 µJ cm^{-2} it can be observed that the broadened and blueshifted emission preserves the radiation pattern, which is related to the idea of temporal lasing peak broadening discussed above (Figure 4d).

To model the observed phenomena of EPs we calculate the eigenvalues and spectral density of the optical modes, which can be estimated as an imaginary part of Green's function, $S(\omega, k_x) = Im(\hat{G}(\omega, k_x))$ identified as $\hat{G}(\omega, k_x) = (\omega - \hat{H}(k_x))^{-1}$, where ω is the frequency and $\hat{H}(k_x)$ is the Hamiltonian of the metasurface cavity modes and can be written as:[22,56,57]

$$\hat{H}(k_x) = \begin{pmatrix} E_+(k_x) & U \\ U & E_-(k_x) \end{pmatrix} - i \begin{pmatrix} \gamma_{nr}(k_x) + \gamma_r & \gamma_r \\ \gamma_r & \gamma_{nr}(k_x) + \gamma_r \end{pmatrix} \quad (3)$$

where $E_{+,-}(k_x)$ stands for the real part of the leaky mode dispersion with positive and negative group velocity, respectively, $\gamma_{nr, r}$ stands for the non-radiative and radiative losses, respectively, and U stands for the coupling coefficients between modes. We extract mode centers and linewidths from the experimental data, shown before. As we do not observe the splitting between two modes at $k_x/k_0 = 0$, we take parameter U equal to zero. EPs appear in the system when the eigenvalues of the Hamiltonian coalesce:

$$\hat{H}\mathbf{a} = \lambda\mathbf{a} \quad (4)$$

$$\lambda_1(k_x^{EP}) = \lambda_2(k_x^{EP}) \quad (5)$$

In this case, spectral density $S(\omega^{EP}, k_x^{EP})$ possess artifacts, which are observed in the experiment as lasing points.

The result of the spectral density calculation based on the extracted experimental data in the linear regime is shown in Figure 4e. The "hotspot" at the Γ-point, where $k_x/k_0 = 0$ corresponds to the enhanced spontaneous emission, shown in Figure 4a. Then, we shift the polariton mode in the model as it is observed in the experiment (Figure 4f). To take into account the stimulated emission, we assume that the nonradiative losses can be expressed as the difference between absorption (losses) $\alpha(k_x)$ and gain (stimulated polaritons) $\beta(k_x)$: $\gamma_{nr}(k_x) = \alpha(k_x) - \beta(k_x)$. To estimate the $\beta(k_x)$ we extract the ASE spectrum from the experimental results, shown in Figure 3a, and consider it as a gain $\beta(k_x)$, multiplied by the constant G_0. By varying the parameter G_0 we find the critical conditions when the eigenvalues degenerate and EPs appear (see Section 3, Supporting Information). After applying the calculated gain, which does not exceed the full losses, we observe the sign changing of spectral den-

sity in the particular places near k_x/k_0, which corresponds to the EPs. As EPs are the specific state, which is very sensitive to the variation of the parameters,[17] it has to be destroyed after the higher $\beta(k_x)$ under higher fluences. However, thanks to the polariton nature, in the regime of the polariton condensation in EPs, all new polaritons which scatter under a higher pump rapidly recombine and do not produce the change of the imaginary part of the mode.

3. Conclusion

In summary, we have demonstrated room-temperature polariton lasing mediated by the EPs in the perovskite-based non-local metasurface. Along with the solution-processable perovskite synthesis methods, the nanoimprint lithography provides large-area gratings supporting high-Q modes (up to Q≈2300) formed by symmetry-protected BIC and the EPs in the active nonlinear regime. We have revealed that the ASE in the studied samples originates from the accumulation of polaritons in the spectral region with the excitonic fraction in polariton of around 0.3. With further increase of the carrier concentration, the ASE broadens towards the red region due to the polariton relaxation, and EPs appear when the metasurface modes are crossed within the gain spectral range. Our results explain the fundamental origin of the lasing in lead-bromide metasurfaces and open new ways for the realization of room-temperature planar polariton lasers based on a rich variety of halide perovskites. Since the proposed cavity design is close to the most optimal case, we envision further lasing thresholds lowering through the material properties optimization via the synthesis of highly crystalline perovskite films[58–60] and cation engineering,[61] which can lead to low-cost continuous wave[62,63] and electrically pumped lasers,[64] essential for industrial applications.

4. Experimental Section

Perovskite Metasurface Fabrication: The fabrication process was divided into three main steps: solution preparation, thin film spin-coating, and nanoimprint lithography. First, the perovskite solution was prepared in the dry N$_2$ glove box by the mixture of 33.59 mg of MABr (TCI) and 110.1 mg of PbBr$_2$ (TCI). Then it was dissolved in a 1 mL mixture of DMF and DMSO in a ratio of 3:1 and steered by a magnetic stirrer for 24 h. Second, substrates of SiO$_2$ were cleaned by consistent sonication in deionized water, acetone, and isopropanol for 10 min. After it is dried out and put into the plasma cleaner for 10 min to achieve high surface adhesion. Cleaned substrates were transferred to the dry N$_2$ glove box, where further film deposition is provided. The perovskite film synthesis starts with the deposition of 30 µL MAPbBr$_3$ solution on the cleaned substrate and then the spin-coater starts the rotation. The substrate with a deposited solution is spun for 50 s with a speed rotation of 3.000 or 3.500 rates per minute (rpm), depending on the target film thickness. At the 35th s, after the rotation starts, 300 µL of the antisolvent (toluene) was dripped at the top of the rotated substrate to remove the solution and cause fast and uniform film crystallization. The surface morphology, XRD patterns, and absorbance spectrum are in good agreement with previous works[50,65] and were shown in Figures S11, S12, and S13 (Supporting Information), respectively. At the third stage of the synthesis substrate with perovskite film in the intermediate phase

before thermal annealing was transferred to a laboratory press for the nanoimprint lithography. The mold for the nanoimprint represents the periodic grating with a period of 320 nm, a comb height of 25 nm, and a ratio between comb width and structure period (FF) of 0.5, made of polycarbonate. The perovskite film with the mold on the top is located in the laboratory press, where the pressure of around 200 MPa is applied for 10 min. After the mold is removed, the substrate with the perovskite imprinted film was annealed at 90 °C for 10 min in the atmosphere of the dry N_2 glove box.

Angle-Resolved Spectroscopy: Angle-resolved spectroscopy measurements were performed with a back-focal-plane (BFP) 4f setup by using a slit spectrometer, coupled to the imaging EMCCD camera (Andor Technologies Kymera 328i-B1 + Newton EMCCD DU970P-BVF) and a halogen lamp, coupled to the optical fiber with the collimation lens, employed for the white light illumination. Olympus Plan Achromat Objective with a magnification of 10x and numerical aperture of 0.25 was used for the excitation and collection of the signal. Spatial filtering was carried out in the intermediate image plane (IP), transferred by the 4f scheme. The polarization was filtered by a linear polarizer after the spatial filter. Angle-resolved photoluminescence measurements were performed in the same setup by using the femtosecond (fs) laser with a wavelength of 400 nm and a repetition rate of 1 kHz. The laser system represents mode-locked Ti:sapphire laser at 800 nm, which was used as a seed pulse for the regenerative amplifier (Spectra Physics, Spitfire Pro), and then is frequency-doubled via BBO crystal. A lens with a focal distance of 500 mm was used to focus the laser beam in the BFP to achieve a large pump spot of around 175 μm. To filter the laser in the collection channel long-pass filter FEL450 was used. A CCD camera (Thorlabs 1.6 MP Color CMOS Camera DCC1645C) with a 150 mm tube lens after the beamsplitter in the collection channel was used for the imaging of the real and Fourier space. The experimental scheme was shown in Figure S1 (Supporting Information).

Supporting Information

Supporting Information is available from the Wiley Online Library or from the author.

Acknowledgements

Conflict of Interest

The authors declare no conflict of interest.

Data Availability Statement

The data that support the findings of this study are available from the corresponding author upon reasonable request.

[1] D. Sanvitto, V. Timofeev, *Exciton Polaritons in Microcavities: New Frontiers*, vol. 172, Springer, Berlin **2012**.

[2] H. Deng, G. Weihs, C. Santori, J. Bloch, Y. Yamamoto, *Science* **2002**, *298*, 199.

[3] J. Kasprzak, M. Richard, S. Kundermann, A. Baas, P. Jeambrun, J. M. J. Keeling, F. Marchetti, M. Szymańska, R. André, J. Staehli, V. Savona, P. B. Littlewood, B. Deveaud, L. Si Dang, *Nature* **2006**, *443*, 409.

[4] H. Deng, G. Weihs, D. Snoke, J. Bloch, Y. Yamamoto, *Proc. Natl. Acad. Sci. USA* **2003**, *100*, 15318.

[5] C. Weisbuch, M. Nishioka, A. Ishikawa, Y. Arakawa, *Phys. Rev. Lett.* **1992**, *69*, 3314.

[6] H. Deng, H. Haug, Y. Yamamoto, *Rev. Mod. Phys.* **2010**, *82*, 1489.

[7] E. Estrecho, T. Gao, N. Bobrovska, D. Comber-Todd, M. D. Fraser, M. Steger, K. West, L. N. Pfeiffer, J. Levinsen, M. Parish, T. C. H. Liew, M. Matuszewski, D. W. Snoke, A. G. Truscott, E. A. Ostrovskaya, *Phys. Rev. B* **2019**, *100*, 035306.

[8] S. Christopoulos, G. B. H. Von Högersthal, A. Grundy, P. Lagoudakis, A. Kavokin, J. Baumberg, G. Christmann, R. Butté, E. Feltin, J.-F. Carlin, N. Grandjean, *Phys. Rev. Lett.* **2007**, *98*, 126405.

[9] R. Su, C. Diederichs, J. Wang, T. C. Liew, J. Zhao, S. Liu, W. Xu, Z. Chen, Q. Xiong, *Nano Lett.* **2017**, *17*, 3982.

[10] R. Su, J. Wang, J. Zhao, J. Xing, W. Zhao, C. Diederichs, T. C. Liew, Q. Xiong, *Sci. Adv.* **2018**, *4*, eaau0244.

[11] S. Betzold, M. Dusel, O. Kyriienko, C. P. Dietrich, S. Klembt, J. Ohmer, U. Fischer, I. A. Shelykh, C. Schneider, S. Hofling, *ACS Photonics* **2019**, *7*, 384.

[12] K. Koshelev, A. Bogdanov, Y. Kivshar, *Sci. Bull.* **2019**, *64*, 836.

[13] A. Overvig, A. Alù, *Laser Photonics Rev.* **2022**, *16*, 2100633.

[14] V. Kravtsov, E. Khestanova, F. A. Benimetskiy, T. Ivanova, A. K. Samusev, I. S. Sinev, D. Pidgayko, A. M. Mozharov, I. S. Mukhin, M. S. Lozhkin, Y. V. Kapitonov, A. S. Brichkin, V. D. Kulakovskii, I. Shelykh, A. I. Tartakovskii, P. M. Walker, M. S. Skolnick, D. N. Krizhanovskii, I. Iorsh, *Light: Sci. Appl.* **2020**, *9*, 1.

[15] K. Koshelev, S. Sychev, Z. F. Sadrieva, A. A. Bogdanov, I. Iorsh, *Phys. Rev. B* **2018**, *98*, 161113.

[16] V. Ardizzone, F. Riminucci, S. Zanotti, A. Gianfrate, M. Efthymiou-Tsironi, D. Suàrez-Forero, F. Todisco, M. De Giorgi, D. Trypogeorgos, G. Gigli, K. Baldwin, L. Pfeiffer, D. Ballarini, H. S. Nguyen, D. Gerace, D. Sanvitto, *Nature* **2022**, *605*, 447.

[17] M.-A. Miri, A. Alù, *Science* **2019**, *363*, eaar7709.

[18] B. Peng, Ş. K. Özdemir, M. Liertzer, W. Chen, J. Kramer, H. Yılmaz, J. Wiersig, S. Rotter, L. Yang, *Proc. Natl. Acad. Sci. USA* **2016**, *113*, 6845.

[19] T. Goldzak, A. A. Mailybaev, N. Moiseyev, *Phys. Rev. Lett.* **2018**, *120*, 013901.

[20] I. Doronin, A. Zyablovsky, E. Andrianov, A. Pukhov, A. Vinogradov, *Phys. Rev. A* **2019**, *100*, 021801.

[21] A. A. Zyablovsky, I. V. Doronin, E. S. Andrianov, A. A. Pukhov, Y. E. Lozovik, A. P. Vinogradov, A. A. Lisyansky, *Laser Photonics Rev.* **2021**, *15*, 2000450.

[22] L. Lu, Q. Le-Van, L. Ferrier, E. Drouard, C. Seassal, H. S. Nguyen, *Photonics Res.* **2020**, *8*, A91.

[23] A. Pick, B. Zhen, O. D. Miller, C. W. Hsu, F. Hernandez, A. W. Rodriguez, M. Soljačić, S. G. Johnson, *Opt. Express* **2017**, *25*, 12325.

[24] Q. Zhang, T. Krisnanda, D. Giovanni, K. Dini, S. Ye, M. Feng, T. C. Liew, T. C. Sum, *J. Phys. Chem. Lett.* **2022**, *13*, 7161.

[25] H. Shan, I. Iorsh, B. Han, C. Rupprecht, H. Knopf, F. Eilenberger, M. Esmann, K. Yumigeta, K. Watanabe, T. Taniguchi, S. Klembt, S. Höfling, S. Tongay, C. Antón-Solanas, I. A. Shelykh, C. Schneider, *Nat. Commun.* **2022**, *13*, 1.

[26] A. K. Jena, A. Kulkarni, T. Miyasaka, *Chem. Rev.* **2019**, *119*, 3036.

[27] Y. Zhang, C.-K. Lim, Z. Dai, G. Yu, J. W. Haus, H. Zhang, P. N. Prasad, *Phys. Rep.* **2019**, *795*, 1.

[28] R. Su, A. Fieramosca, Q. Zhang, H. S. Nguyen, E. Deleporte, Z. Chen, D. Sanvitto, T. C. Liew, Q. Xiong, *Nat. Mater.* **2021**, *20*, 1315.

[29] H. Huang, M. I. Bodnarchuk, S. V. Kershaw, M. V. Kovalenko, A. L. Rogach, *ACS Energy Lett.* **2017**, *2*, 2071.

[30] R. Su, S. Ghosh, J. Wang, S. Liu, C. Diederichs, T. C. Liew, Q. Xiong, *Nat. Phys.* **2020**, *16*, 301.

[31] Q. Shang, M. Li, L. Zhao, D. Chen, S. Zhang, S. Chen, P. Gao, C. Shen, J. Xing, G. Xing, B. Shen, X. Liu, Q. Zhang, *Nano Lett.* **2020**, *20*, 6636.

[32] K. Peng, R. Tao, L. Haeberlé, Q. Li, D. Jin, G. R. Fleming, S. Kéna-Cohen, X. Zhang, W. Bao, *Nat. Commun.* **2022**, *13*, 1.

[33] R. Tao, K. Peng, L. Haeberlé, Q. Li, D. Jin, G. R. Fleming, S. Kéna-Cohen, X. Zhang, W. Bao, *Nat. Mater.* **2022**, 1.

[34] A. Zhizhchenko, A. Cherepakhin, M. Masharin, A. Pushkarev, S. Kulinich, A. Porfirev, A. Kuchmizhak, S. Makarov, *Laser Photonics Rev.* **2021**, *15*, 2100094.

[35] S. V. Makarov, V. Milichko, E. V. Ushakova, M. Omelyanovich, A. Cerdan Pasaran, R. Haroldson, B. Balachandran, H. Wang, W. Hu, Y. S. Kivshar, A. A. Zakhidov, *ACS Photonics* **2017**, *4*, 728.

[36] J. Feng, J. Wang, A. Fieramosca, R. Bao, J. Zhao, R. Su, Y. Peng, T. C. Liew, D. Sanvitto, Q. Xiong, *Sci. Adv.* **2021**, *7*, eabj6627.

[37] I. A. Al-Ani, K. As' Ham, L. Huang, A. E. Miroshnichenko, W. Lei, H. T. Hattori, *Adv. Opt. Mater.* **2022**, *10*, 2101120.

[38] K. As' ham, I. Al-Ani, W. Lei, H. T. Hattori, L. Huang, A. Miroshnichenko, *Phys. Rev. Appl.* **2022**, *18*, 014079.

[39] N. H. M. Dang, S. Zanotti, E. Drouard, C. Chevalier, G. Trippé-Allard, M. Amara, E. Deleporte, V. Ardizzone, D. Sanvitto, L. C. Andreani, C. Seassal, D. Gerace, H. S. Nguyen, *Adv. Opt. Mater.* **2022**, *10*, 2102386.

[40] S. A. Veldhuis, P. P. Boix, N. Yantara, M. Li, T. C. Sum, N. Mathews, S. G. Mhaisalkar, *Adv. Mater.* **2016**, *28*, 6804.

[41] N. Pourdavoud, A. Mayer, M. Buchmüller, K. Brinkmann, T. Häger, T. Hu, R. Heiderhoff, I. Shutsko, P. Görrn, Y. Chen, H.-C. Scheer, T. Riedl, *Adv. Mater. Technol.* **2018**, *3*, 1700253.

[42] C. Huang, C. Zhang, S. Xiao, Y. Wang, Y. Fan, Y. Liu, N. Zhang, G. Qu, H. Ji, J. Han, L. Ge, Y. Kivshar, Q. Song, *Science* **2020**, *367*, 1018.

[43] A. Palatnik, C. Cho, C. Zhang, M. Sudzius, M. Kroll, S. Meister, K. Leo, *Adv. Photonics Res.* **2021**, *2*, 2100177.

[44] N. J. Jeon, J. H. Noh, Y. C. Kim, W. S. Yang, S. Ryu, S. I. Seok, *Nat. Mater.* **2014**, *13*, 897.

[45] M. A. Masharin, V. A. Shahnazaryan, F. A. Benimetskiy, D. N. Krizhanovskii, I. A. Shelykh, I. V. Iorsh, S. V. Makarov, A. K. Samusev, *Nano Lett.* **2022**, *22*, 9092.

[46] M. S. Alias, I. Dursun, M. I. Saidaminov, E. M. Diallo, P. Mishra, T. K. Ng, O. M. Bakr, B. S. Ooi, *Opt. Express* **2016**, *24*, 16586.

[47] L. Li, *JOSA A* **1997**, *14*, 2758.

[48] J. Hopfield, *Phys. Rev.* **1958**, *112*, 1555.

[49] N. Sestu, M. Cadelano, V. Sarritzu, F. Chen, D. Marongiu, R. Piras, M. Mainas, F. Quochi, M. Saba, A. Mura, G. Bongiovanni, *J. Phys. Chem. Lett.* **2015**, *6*, 4566.

[50] A. M. Soufiani, F. Huang, P. Reece, R. Sheng, A. Ho-Baillie, M. A. Green, *Appl. Phys. Lett.* **2015**, *107*, 231902.

[51] J. Shi, J. Li, J. Wu, H. Wu, Y. Luo, D. Li, J. J. Jasieniak, Q. Meng, *Adv. Opt. Mater.* **2020**, *8*, 1902026.

[52] M. Masharin, V. Shahnazaryan, I. Iorsh, S. Makarov, A. Samusev, I. Shelykh, **2022**, https://doi.org/10.1021/acsphotonics.2c01773.

[53] A. P. Schlaus, M. S. Spencer, K. Miyata, F. Liu, X. Wang, I. Datta, M. Lipson, A. Pan, X.-Y. Zhu, *Nat. Commun.* **2019**, *10*, 1.

[54] L. Lei, Q. Dong, K. Gundogdu, F. So, *Adv. Funct. Mater.* **2021**, *31*, 2010144.

[55] L. Ferrier, P. Bouteyre, A. Pick, S. Cueff, N. H. M. Dang, C. Diederichs, A. Belarouci, T. Benyattou, J. Zhao, R. Su, J. Xing, Q. Xiong, H. S. Nguyen, *Phys. Rev. Lett.* **2022**, *129*, 083602.

[56] E. Engdahl, E. Brändas, M. Rittby, N. Elander, *J. Math. Phys.* **1986**, *27*, 2629.

[57] A. Vijay, H. Metiu, *J. Chem. Phys.* **2002**, *116*, 60.

[58] W. Du, X. Wu, S. Zhang, X. Sui, C. Jiang, Z. Zhu, Q. Shang, J. Shi, S. Yue, Q. Zhang, J. Zhang, X. Liu, *Nano Lett.* **2022**, *22*, 4049.

[59] N. Pourdavoud, A. Mayer, M. Buchmüller, K. Brinkmann, T. Häger, T. Hu, R. Heiderhoff, I. Shutsko, P. Görrn, Y. Chen, H.-C. Scheer, T. Riedl, *Adv. Mater. Technol.* **2018**, *3*, 1700253.

[60] D. Tatarinov, S. Anoshkin, I. Tzibizov, V. Sheremet, F. Isik, A. Y. Zhizhchenko, A. Cherepakhin, A. A. Kuchmizhak, A. Pushkarev, S. Makarov, *Adv. Opt. Mater.* **2023**, 2202407.

[61] A. L. Alvarado-Leannos, D. Cortecchia, C. N. Saggau, S. Martani, G. Folpini, E. Feltri, M. D. Albaqami, L. Ma, A. Petrozza, *ACS Nano* **2022**, *16*, 20671.

[62] Y. Jia, R. A. Kerner, A. J. Grede, B. P. Rand, N. C. Giebink, *Nat. Photonics* **2017**, *11*, 784.

[63] C. Qin, A. S. Sandanayaka, C. Zhao, T. Matsushima, D. Zhang, T. Fujihara, C. Adachi, *Nature* **2020**, *585*, 53.

[64] T. Wang, Z. Zang, Y. Gao, C. Lyu, P. Gu, Y. Yao, K. Peng, K. Watanabe, T. Taniguchi, X. Liu, Y. Gao, W. Bao, Y. Ye, *Nano Lett.* **2022**, *22*, 5175.

[65] Z. Wang, M. Luo, Y. Liu, M. Li, M. Pi, J. Yang, Y. Chen, Z. Zhang, J. Du, D. Zhang, Z. Liu, S. Chen, *Small* **2021**, *17*, 2101107.

2215007 (10 of 10)